The Impact of Vertical Salinity Gradient on Non-Line-of-Sight Underwater Optical Wireless Communication

Mohammed Sait, *Graduate Student Member, IEEE*, Yujian Guo, *Graduate Student Member, IEEE*, Omar Alkhazragi, *Graduate Student Member, IEEE*, Meiwei Kong, *Member, IEEE*, Tien Khee Ng, *Senior Member, IEEE*, and Boon S. Ooi, *Senior Member, IEEE*

***Abstract*—The non-line-of-sight (NLOS) underwater communication can offer a viable route in signal propagation and coverage, thus mitigating the pointing, acquisition, and tracking difficulties in line-of-sight optical communication. However, implementing the NLOS link is non-trivial. While the NLOS technique relies on light scattering, i.e., channel turbulence can facilitate NLOS communication, the associated path-loss (PL) can be significant. Signal fading can degrade link robustness, which arises due to ocean water temperature and salinity fluctuation and gradients. To evaluate the robustness of NLOS in natural waters, we systematically measure the link metrics, such as the bit error ratio, PL, and signal-to-noise ratio (SNR), of water bodies of uniform and nonuniform vertical salinity ranging from 30–40‰ (part-per-thousand). We found that salinity-induced turbulence can establish NLOS communication with PL reduction of 2.35 dB/m and SNR increase by 32.5% for dynamic water. Furthermore, a strong correlation was obtained between the strength of signal fluctuations and the received SNR. Finally, we obtained a Gaussian distribution of the statistical scintillation behavior. These results demonstrated the benefit of using the NLOS regime for underwater wireless sensor networks for aiding designers and engineers.**

***Index Terms*—Non-line-of-sight, turbulence, salinity, underwater optical communication.**

I. Introduction

AT PRESENT, the oceanic medium serves as the spine of data transmission, connecting the world via fiber-optic cables. In addition, crude oil, which plays a significant role in energy resources, is transferred through pipelines in the ocean. Deploying, maintaining, and monitoring around 406 submarine cables [1] and pipelines is a labor-intensive, expensive, and critical job protecting aquatic life. Hence, it is essential to establish reliable underwater wireless sensor networks for marine environmental monitoring, ecological protection, and scientific research. For years, acoustic technology has been embraced as the primary approach for establishing underwater connectivity between objects. However, the ceaseless demand for high-data-rate transmission for multimedia applications has pushed acoustic technology beyond its limits. Although communication distances extend to many kilometers, the high latency due to slow propagation speed, multipath propagation, and Doppler spread naturally restricts acoustic technology's throughput [2]. Radio frequency (RF) waves can overcome the aforementioned drawbacks, but they are dramatically attenuated underwater, thus limiting their propagation distances to only a few meters [3]. In contrast, optical waves offer high bandwidth, low latency, and high capacity [4]. However, the interaction of light with non-homogeneous random media, such as seawater, is complex. Absorption and scattering are the main factors responsible for deteriorating underwater wireless optical communication (UWOC). When a signal is prematurely absorbed due to the interaction with water molecules, phytoplankton and both organic and inorganic (e.g., salt) suspended particles, the photon energy is converted into other forms of energy, such as heat or kinetic energy. Scattering is the process whereby the photon changes its optical path due to collisions with water molecules, resulting in a reduction in received power at the endpoint.

Light propagation in the aquatic medium also suffers from turbulence-induced fading, which arises from variations in the refractive index along the propagation path and contributes to severe communication performance degradation. Such variations in the refractive index can be attributed to temperature, different salinity concentrations, and the presence of air bubble clouds. Temperature disparities can cause beam wandering, which alters the strict alignment of the transmitter and the receiver [5]–[7]. Further, air bubbles deteriorate the quality of the received signal by increasing the prevalence of scattering events and blockages [8]–[10].

In natural water, salinity significantly contributes to underwater turbulence, causing variations in the water medium's refractive index. Salt elements such as NaCl, KCl, MgCl, $MgSO_4$, and $CaSO_4$ make the principal contributions to the absorption of

Manuscript received September 13, 2021; revised October 10, 2021; accepted October 14, 2021. Date of publication October 19, 2021; date of current version November 9, 2021. This work was supported in part by King Abdullah University of Science and Technology under Grants BAS/1/1614-01-01, KCR/1/2081-01-01, KCR/1/4114-01-01, and GEN/1/6607-01-01, and in part by King Abdulaziz City for Science and Technology under Grant KACST TIC R2-FP-008. *(Corresponding author: Boon S. Ooi.)*

The authors are with the Photonics Laboratory, Computer, Electrical, and Mathematical Sciences and Engineering Division, King Abdullah University of Science and Technology, Thuwal 21534, Saudi Arabia (e-mail: mohammed.sait@kaust.edu.sa; yujian.guo.1@kaust.edu.sa; omar.alkhazragi@kaust.edu.sa; meiwei.kong@kaust.edu.sa; tienkhee.ng@kaust.edu.sa; boon.ooi@kaust.edu.sa).

Digital Object Identifier 10.1109/JPHOT.2021.3121169

TABLE I
LITERATURE REVIEW ON THE EXPERIMENTAL WORK CONCERNING THE STUDY OF TURBULENCE IN THE PAST THREE YEARS. TW STANDS FOR THIS WORK

Ref	ConFig.	Turbulence parameter	Contribution	Year
TW	NLOS	Salinity	Shows that salinity induced turbulence have positive effect on NLOS communication	2021
[11]	LOS	Temperature and salinity	Studied turbulent flow under temperature and salinity variations	2021
[12]	LOS	Surface waves	Showed that surface wave increases scattering of the optical beam	2020
[13]	LOS	Salinity	Showed that turbulent saline flow degrades the communication performance	2020
[14]	LOS	Temperature	Investigated aperture averaging in thermal turbulence and provided statistical model	2020
[15]	LOS	Salinity	Investigated the effect of salinity on received optical power	2020
[16]	LOS	Temperature and salinity	Studied the relationship between transmission depth and turbulence	2020
[17]	LOS	Algae	Examined the effect of moving microalgae on optical links	2020
[18]	LOS	Temperature	vehicle-motion via the turbulent kinetic energy	2020
[9]	LOS	Air bubbles	Investigated the effect of air bubbles on received intensity fluctuation	2019
[19]	LOS	Temperature	Studied the wavelength dependence on turbulence and showed longer wavelengths are more resilient to turbulence	2019
[20]	NLOS	Temperature and air bubbles	Showed that NLOS configuration benefits from oceanic turbulence	2019
[21]	LOS	Maalox, chlorophyll and salinity	Showed that turbidity, and salinity are responsible for worsening the communication performance	2019

electromagnetic radiation in the water [22]. Given that salinity causes reduction in the signal-to-noise ratio (SNR) and hence an optical power-loss [15], it is also responsible for an increase in the scattering coefficient [23], [24]. The effect of multiple absorbing and scattering agents, such as Maalox, chlorophyll, and sea salt, on UWOC channels has been studied in [21]. Increasing the salt concentration was found to increase the attenuation coefficient by increasing the scattering coefficient. Other experimental studies have been carried out to assess and model the underwater optical channel in the presence of salinity [25]. For instance, the Weibull model was used to characterize the fading of salinity-induced turbulence in UWOC channels [26], and generalized gamma and exponentiated Weibull distributions were found to model the fading statistics perfectly [27]. Previous studies have shown that uniform saline channels induce greater turbulence when subjected to turbulent flow due to the faster variations in the refractive index along the optical path [13].

Over the past years, turbulence studies have become a point of interest for researchers to develop accurate models for the propagation and interaction of light with water [28]. Such models aid the prediction of the performance of communication without the need for physical deployments. However, most of these works are based on the line-of-sight (LOS) geometry. Table I shows the turbulence studies over the past three years.

Several novel solutions can be adopted to build robust UWOC links that are resilient to underwater turbulence, such as employing optical receivers with large detection areas [29]. In addition, the implantation of non-line-of-sight (NLOS) configurations combats channel impairments and eases the requirement of strict positioning, acquisition, and tracking while providing high-speed connectivity [30], and resilience to turbulence [20]. Despite its advantages over LOS, it is rarely explored by researchers, as evident from Table I.

Scattering due to salinity is expected to be more pronounced, resulting in enhanced received power. Although it could be expected that turbulence can cause fading (i.e., lowering the signal quality) and that the random scattering can improve the NLOS received power, it is not trivial to know whether the overall effect would result in a better or worse performance. This paper aims to answer this question by stating that the performance is improved in the tested conditions due to the compensation of SNR.

II. EXPERIMENTAL CONSIDERATIONS

A. Evaluation Metrics

We use three performance metrics to evaluate the effect of salinity on NLOS channels, namely the bit error ratio (BER), SNR, path-loss (PL), which is expressed as:

$$PL = 10\log_{10}\left(\frac{P_t}{P_r}\right) \tag{1}$$

where P_t is the transmitted optical power and P_r is the received optical power. Further, to quantify the fading strength, we measure the scintillation index of the propagating light wave as:

$$\sigma_I^2 = \frac{E[I^2] - E^2[I]}{E^2[I]} \tag{2}$$

where I is the instantaneous intensity and $E[\cdot]$ denotes the ensemble average of a random variable. We characterize the obtained results by determining the statistical distribution, and examined their accuracy in terms of goodness-of-fit (GoF). This provides a method evaluating the difference between the data obtained from an experiment and the theoretical statistical distribution obtained from the associated probability density function (PDF). The GoF, which is also referred to as the R^2 measure, is defined as:

$$R^2 = 1 - \frac{\sum_i (y_i - f_i)^2}{\sum_i (y_i - \bar{y})^2}, \quad 0 < R^2 < 1, \tag{3}$$

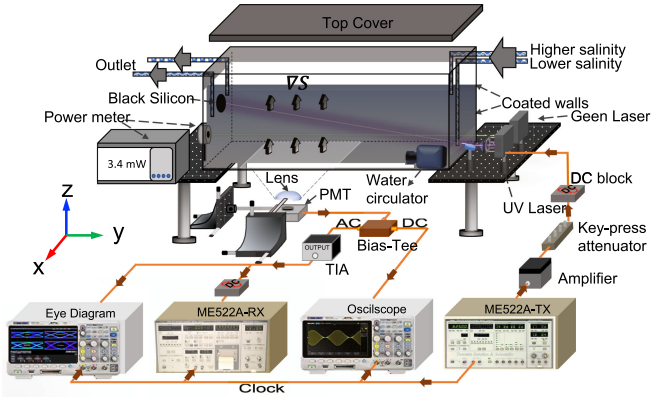

Fig. 1. Experimental setup for NLOS communication with salinity-induced turbulence. Two water inlets with different salinity concentrations are injected from the right side of the tank. The water with a higher salt concentration is injected at the top layer of the water tank, while the lower salt concentration is injected at the bottom of the tank. The salinity gradient, labelled ∇S, is formed vertically as indicated by the arrows. Two outlet tubes at the left side of the tank withdraw the water mixture from the middle of the tank at the same rate as the water injection to maintain a constant water level.

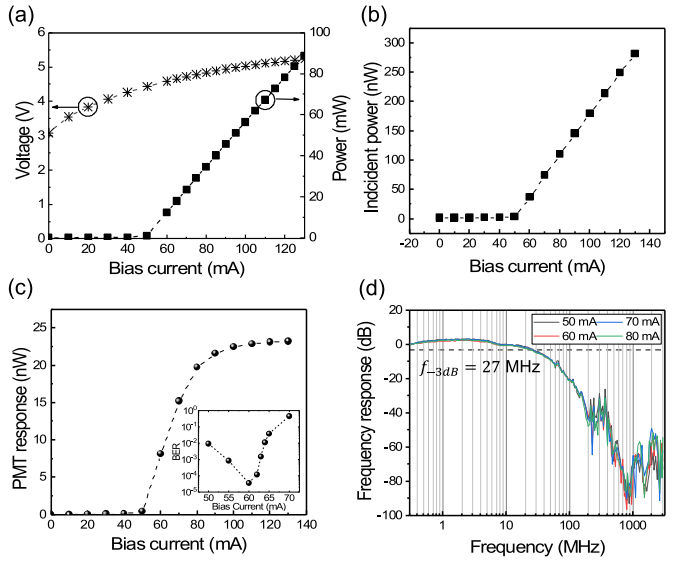

Fig. 2. (a) Laser L–I–V curve. (b) Received incident power in the plane of the photomultiplier tube (PMT), measured via a power meter in coastal water with salt-free medium. (c) PMT response after matching. (d) The frequency response of the system. The dashed line indicates the −3-dB bandwidth.

where i is the bin number, y_i and f_i are the measured and predicted probability values, respectively, for a given received intensity level corresponding to the ith bin, and $\bar{y}$ is the mean of the measured intensity values.

B. Experimental Setup

Fig. 1 shows the experimental setup designed for this study. We utilized a water tank with dimensions of $43 \times 27 \times 26$ cm^3. The water tank was placed at the edges of two optical tables, while the bottom of the tank was mostly free, as shown in the figure. The water tank was filled with coastal water (i.e., the attenuation coefficient of 0.398 m^{-1}) by adding a controlled amount of Maalox as a scattering agent. We placed a single-mode pigtailed green laser light (Thorlabs LP520SF15) at one side of the tank and a power meter (Newport 2936-R) with a photodetector (UV-818) at the other end of the tank and maintained the water type by monitoring the output power from the water tank. This is because the Maalox particles dissolve in water over time, and so, small volumes of Maalox were added according to the output power of the green laser light. We used the Beer–Lambert law to calculate the output power required to maintain the water's attenuation coefficient:

$$I_{Maalox} = I_{Pure} \exp[-d(\alpha_{Maalox} - \alpha_{Pure})] \qquad (4)$$

where I_{Maalox} (mW) is the measured intensity of the laser light after propagating through the coastal water, I_{Pure} is the intensity of light when only distilled water is added (i.e., no Maalox), d is the distance of the optical path along the width of the tank, α_{Pure} is the attenuation coefficient when only distilled water is added (this takes into account other intensity degradation factors, such as the refraction of light ascribed to the presence of glass and water mediums), and α_{Maalox} is the attenuation coefficient of the water type to be maintained.

The NLOS configuration relies on scattered photons to reach the receiver after single or multiple scattering events. To enhance the scattering events, the NLOS configuration usually uses wavelengths in the ultraviolet (UV) spectrum [31], [32]. Therefore, at the transmitter side, a UV laser (Thorlabs L375P70MLD) was utilized as a transmitter, with a maximum optical output power of 85 mW and peak wavelength of 377 nm. For cooling, a Thorlabs (TCLDM9) and a thermoelectric controller (TEC, Thorlabs ITC4001) were mounted on and connected to the laser-diode module. The L–I–V characteristic curve of the laser is shown in Fig. 2(a). From the figure, we can observe that the laser has a turn-on voltage of 3.078 V and a threshold current of 50 mA. In this study, we limited the maximum operating current to 130 mA to avoid damaging overwhelming the laser. The laser was modulated with a non-return-to-zero on-off keying (NRZ-OOK) modulation scheme. Using a pattern generator (ME-522 A Transmitter), a pseudorandom binary sequence (PRBS) was generated with a length of $2^{10} - 1$ bits and fed to the laser's RF port through an amplifier (Mini Circuits ZHL-6A+), a key-press variable electrical attenuator (SMA KT2.5-60) was employed to control the signal's voltage and, lastly, a direct current (DC) block was used to filter out any excess DC voltage generated from the test equipment. The attenuator's keys were selected to output a peak-to-peak alternating current (AC) signal voltage of 2.9 V, which utilizes the laser's extensive dynamic range. The laser beam was collimated using a UV-anti-reflection coated collimation lens that impinges the collimated beam on a mirror (Thorlabs, PF10-03-F01) to control the angle at which the ray enters the water medium.

At the end of the water tank, a nano-fabricated black-silicon wafer [33], a vital component in this experiment, absorbs the incident ray to ensure that the photons at the receiver are entirely due to scattering and not a reflection from the sidewalls. Fig. 3 shows the reflectance of the black-silicon wafer with different incident angles. An incident angle of 40° produces the least

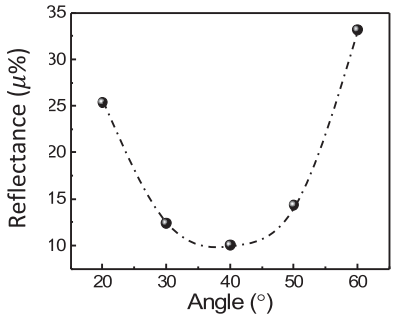

Fig. 3. The reflectance of a black silicon wafer with respect to the angle of incidence.

reflectivity; hence, we adjusted the laser mirror to direct the beam at an angle of 40°. Further, to diminish any reflection from the side walls, we covered the inner walls of the tank with a black coat with reflectivity spectra determined in [20]. We placed a top cover with the same black coat at the top side of the tank to diminish any reflection from the water-air interface and minimize the ambient noise.

At the bottom of the tank, a window slot was cropped from the black coat to allow the scattered rays to enter a photomultiplier tube (PMT, Hamamatsu, R955) via focusing optics (Thorlabs, ACL 7560U-A) with a large diameter of 75 mm for aperture averaging. The PMT is highly sensitive in the UV range, with an anode sensitivity of 7×10^5 A/W at 377 nm. The gain of the PMT can be adjusted by controlling its gain voltage. Higher gain voltages allow for higher amplification, hence lower bandwidth, due to increased response time. The gain voltage in this study was kept at a minimum (2 V) considering that the available scattered intensity-modulated signal was already sufficient to saturate the PMT due to the water tank's limited dimensions. Because the PMT is a highly sensitive detector, PMT–laser response matching is required to match the dynamic range of the laser with the PMT. To do so, we need to know the incident received power after propagating in the water medium at the PMT side with respect to the laser drive current. Therefore, we replaced the PMT with power meter and measured the received power versus the laser drive current. Fig. 2(b) shows the measured received incident power with respect to the drive current of the laser. The curve follows the laser's L–I curve but is attenuated by the salt-free coastal water channel. To match the PMT, we need to calculate the maximum allowable received power at the chosen control voltage. The maximum allowable incident power can be calculated as:

$$P_{PMT(max)} = \frac{I_{out}}{(\eta(\lambda) S_k(\lambda) Gain)}, \tag{5}$$

where I_{out} is the output photocurrent from the PMT, $\eta(\lambda)$ is the quantum efficiency, which depends on the wavelength λ (0.25 at 377 nm), Gain is a multiplication factor that depends on the controlled voltage (1×10^5 at a control voltage of 2 V), and S_k (λ) is the cathode sensitivity of the PMT, defined as the generated photocurrent divided by the incident optical power at the PMT input plane ($70\,\mathrm{mA/W}$ at 377 nm). Under these conditions, the PMT's maximum input power is 24.72 nW. The L–I curve in Fig. 2(b) indicates the incident power from the laser, after propagating through the aquatic channel, is much higher than the maximum allowable input power of the PMT. Therefore, we calculated the neutral-density filter (NDF) value to match the laser and PMT dynamic ranges as NDF≈ 1. The matched PMT response shown in Fig. 2(c) indicates that the PMT exhibits a threshold drive current of 50 mA, then saturates at a drive current of 80 mA. A linear region appears from 50–80 mA, and this can be matched to the laser characteristic curve. The PMT has a measured bandwidth of 37 MHz. Both the PMT and the focusing lens were held by two translational stages, allowing the alignment of the lens and the PMT to be adjusted in the x-y-z directions. The optimal alignment is achieved when the PMT outputs the maximum voltage amplitude at the oscilloscope (Tektronix, MDO3104). Once the PMT detects the signal, it passes through a Bias-Tee (Tektronix, PSPL5541 A), which separates the AC and DC parts of the signal. The AC signal is fed to a trans-impedance amplifier (Hamamatsu, C6438-01) with a gain of 24 mV/μA, which also converts the current signal to a voltage signal. The voltage signal is fed to the ME-522 A receiver through a DC block and a digital communication analyzer (Agilent Technology, 86100 C) for BER calculations and eye-diagram analysis, respectively. A synchronization clock is connected between the ME-522 A transmitter and ME-522 A receiver, as well as between the ME-522 A transmitter and the digital communication analyzer. Moreover, it is crucial to select the optimal operating current for the laser to obtain the best communication performance. Thus, we measured the BER values while sweeping across different drive currents. The inset of Fig. 2(c) shows that a bias current of 60 mA achieves the minimum BER value. Therefore, we used a drive current of 60 mA throughout the experiments. Finally, we examined the bandwidth of the whole system using a Microwave Network Analyzer (Agilent Technology, E8361 C) at different drive currents. The measured bandwidth of the system, shown in Fig. 2(d), indicates a -3-dB bandwidth of 27 MHz. Considering that the laser and PMT have bandwidths of 400 MHz and 37 MHz, the overall system's bandwidth is channel-limited. In addition, we can observe that the bandwidth shown in Fig. 2(d) is not affected by the laser drive current.

III. Results and Discussion

A. Effect of Uniform and Gradient Salinity on the PL of NLOS Channel

The salinity distribution in the ocean varies with depth and region. The variations of salinity with depth are caused by evaporation from sunlight, especially at the surface of the water. Therefore, the surface salinity is generally higher than that in deeper regions. Depending on the geographical region, the salinity range can change, with salinity reaching high values of 40‰ in places such as the Red Sea and low values of 10‰ in the Baltic Sea [34]. However, the average salinity in the ocean is about 35‰. Thus, in this study, we used salinity values ranging from 30–40‰, which is a realistic range. First, we added salt to the water tank and stirred it for around 3 minutes with a

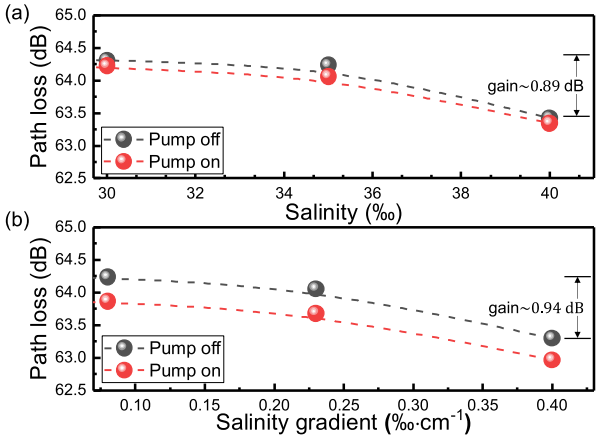

Fig. 4. (a) PL in uniform salinity channel with and without water circulation. (b) PL in salinity gradient channel with and without water circulation.

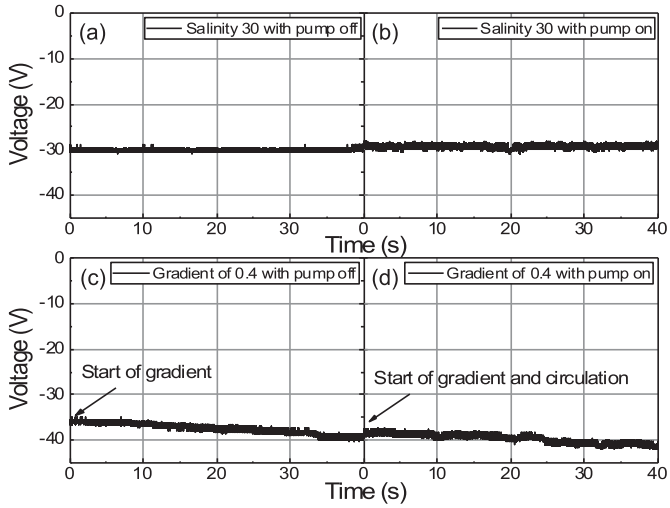

Fig. 5. Received DC optical signal through uniform salinity of 30‰ when the pump is (a) off and (b) on. Received DC optical signal through salinity gradient of 0.4‰·cm^{-1} when the pump is (c) off and (d) on.

circulating pump to dissolve all the salt particles in the water. This procedure was repeated to produce salinity values of 30‰, 35‰, and 40‰. We confirmed that these salinity values were achieved in the water medium using a refractometer salinity sensor (Agriculture Solutions, WL0020-ATC). Furthermore, we created a vertical salinity gradient by filling the water tank with water of average salinity (i.e., 35‰). We should note that we focus on the vertical salinity as the salinity distribution on the ocean is mainly distributed vertically. However, horizontal salinity would also follow the same results presented in the work. We inject two coastal water using two inlet tubes, each with the desired salt concentrations, into the water tank to create gradient levels. We injected the water with the higher salinity concentration at the top of the tank and the less saline water at the bottom of the tank as shown in Fig. 1. To balance the salinity gradient, we placed an outlet tube in the middle of the tank so that the overall water level remained constant. Thus, we obtained salinity gradients of 0.08‰· cm^{-1}, 0.23‰· cm^{-1}, and 0.4‰· cm^{-1}, corresponding to bottom and top salinity levels of 34–36‰, 32–38‰, and 30–40‰, respectively. All measurements were conducted in a dark room at room temperature of 20 °C.

Fig. 4(a) shows the PL measurements for the different salinity values. We can clearly see that increasing the salinity concentration causes a reduction in PL. Additionally, circulating the water medium causes a slight reduction in PL compared with when the water is still. This is reasonable because the water circulation causes the scattering particles in the water to move and the saline regions in the water medium to mix, which causes greater variations in the refractive index, hence enhanced scattering. Fig. 4(b) illustrates the PL measurements for the different salinity gradients. Again, we observe a similar trend, where PL decreases as the salinity gradient increases. In addition, we can see that the water circulation has a more pronounced effect in the case of the salinity gradient than when the salinity is uniform. For example, in the salinity gradient scenario, there is a gain of approximately 2.35 dB/m when the water is circulating.

Figs. 5(a)–(d) show the received optical DC signal in the presence of uniform salinity with turbulent water and a salinity gradient in still and turbulent water, respectively. For the sake of brevity, we do not include all the waveforms of the received signals through the uniform and gradient salinity, but we consider one scenario for each. From the waveform in Fig. 5(a), we can observe that the received signal through a uniform salinity of 30‰ in calm water has almost constant voltage over a 40-s period. However, when water circulation is introduced, scintillation affects the received signal, as shown in Fig. 5(b), which enhances the averaged received power. This explains the reduction in PL in the cases with still and turbulent water, as in Fig. 4(a). Moreover, the salinity gradient channel of 0.4‰· cm^{-1} with still water, shown in Fig. 5(c), indicates that the received signal increases with time as the salinity gradient begins to build up along the vertical direction. Because the water is still, the waveform is almost immutable. However, when circulation is introduced, as in Fig. 5(d), we can observe that the signal has a higher voltage than in the still water scenario, and it fluctuates with time, enhancing the average received power. This is also evident from the PL measurements in Fig. 4(b).

B. Effect of Uniform and Gradient Salinity on NLOS Communication

To test our hypothesis regarding the communication performance, we considered the AC part of the received optical signal. We measured the BER performance as the data communication rate increases under the different conditions of uniform salinity and a salinity gradient. For these measurements, the ME-522 A receiver was set to receive the same number of transmitted bits. However, we selected the complementary PRBS (i.e., $\overline{\text{PRBS}}$) because the PMT outputs negative signals. The clock offset and the detection threshold were adjusted for each measurement to achieve the lowest BER. Adjusting the clock offset was crucial as the scattering events induced a time offset in the received signal.

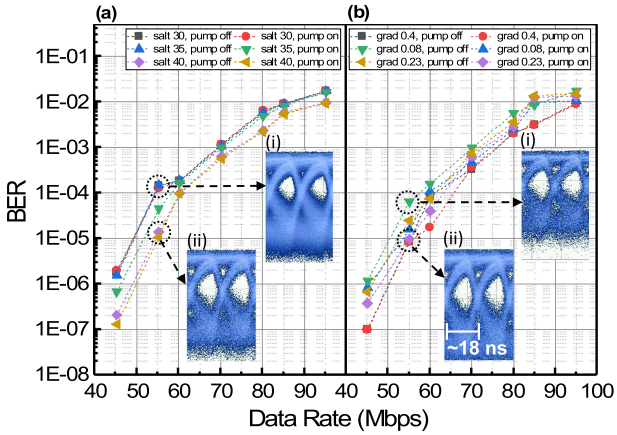

Fig. 6. Measured BER versus data rate in (a) uniform salinity channel. Inset Fig. (i) corresponds to the eye diagram of 30‰ in still water, while (ii) corresponds to the eye diagram of 40‰ in still water. (b) Salinity gradient channel. Inset Fig. (i) corresponds to the eye diagram of 0.08‰·cm^{-1} in still water while (ii) corresponds to the eye diagram of 0.4‰· cm^{-1} in still water.

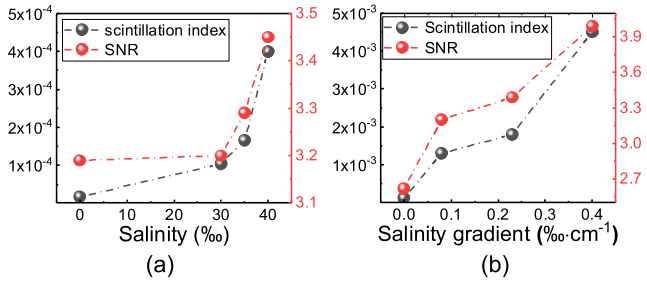

Fig. 7. SNR and scintillation index as a function of (a) uniform and (b) gradient salinity.

This is due to the increase in the time spread. In real systems, the communication is usually done by sending a preamble symbol that is known to the transmitter and the receiver before sending the actual data stream. This training symbol allows for obtaining various parameters such as the channel coefficient and the clock offset (i.e., synchronization). Additionally, in practical system, a fixed data rate is usually adopted. Therefore, a lookup table can be used that records the clock offset for each data rate. We set the error interval period to 1 s so that we received different measurements at different times, then averaged the measurements.

Fig. 6(a) shows that the BER value increases logarithmically as the data rate increases. From the figure, we can observe that, for all channel conditions, circulating the water (i.e., pump on) causes a slight reduction in the BER. Increasing the salt concentration also reduces the BER. For the sake of brevity, we have only included the eye diagrams for salt concentrations of 30‰ and 40‰ for the still water condition, at a data rate of 55 Mbit/s, in the inset of Fig. 6(a). The insets indicate that increasing the salt concentration increases the eye's height by enhancing the SNR. Fig. 6(b) illustrates the BER measurements in the case of a salinity gradient in the water channel. Increasing the salinity gradient reduces the BER values, and water circulation further decreases the BER as a consequence of increasing the SNR. We can also observe that the BER values are spread further apart in the BER axis. This indicates that water circulation, which arises from the ocean's currents and tides, in the presence of a salinity gradient has a greater effect in enhancing the communication quality than when the water medium has a homogeneous salt concentration. In addition, by observing the eye diagrams in Fig. 6(b), we can observe a similar trend whereby the eye's height increases as a result of increasing the gradient level. We did not consider the effect of the water flow rate on the characterization. However, we anticipate that the flow rate also enhances the communication link, because a faster water flow would induce stronger signal scintillation.

To further understand the correlation between the performance of the NLOS link in saline water and the strength of turbulence, we measured the scintillation index and SNR for different salt concentrations in the presence of water circulation. We did not consider the still water case, because still saline water does not induce much turbulence. Fig. 7(a) shows that the SNR for the communication channels increases with the salinity concentration. It can be noted that the SNR has increased by about 7.2‰.

Fig. 7(b) shows the relationship between the scintillation index, SNR and salinity gradient in turbulent water scenario. We can observe a similar trend whereby the SNR is strongly correlated to the strength of signal fluctuations. In addition, an increase of 32.5‰ is observed. We can also notice that the salinity gradient induces an order of magnitude increase in the scintillation index compared with homogeneous saline channels. This is still considered as a weak-turbulence regime, even though the salinity gradient ranges in this study were extreme. However, the SNR gain is not markedly different. This could be attributed to the increase in ISI when the scattering is enhanced by the salinity gradient and the dynamic water. However, further experimental investigation is required to verify the effect of ISI in such case. Due to the positive correlation of SNR with the scintillation index, we can conclude that saline water induces an overall beneficial effect on the communication performance.

C. Modeling NLOS Channel Under Salinity Induced-Turbulence

Modeling the underwater channel is crucial to making statistical predictions of the received signal behavior. To model the NLOS underwater channel in the presence of salinity-induced turbulence, we computed histograms of the experimental data, then fitted them to three statistical distributions (normal, log-normal, and Weibull). For each histogram, we measured three data points and measured the average values. Figs. 8(a)–(h) show the histograms of the received signal fluctuations when the pump is on and off for all salt concentrations. The number bins were fixed for all histograms. However, the low number of data occurrence is attributed to two reasons; since the uniform salinity distribution in the still water medium does not induce much fluctuation as seen from Fig. 5(a), we decreased the sampling rate of the oscilloscope to capture longer time intervals. Therefore, due to the decrease in vertical quantization levels, the number of

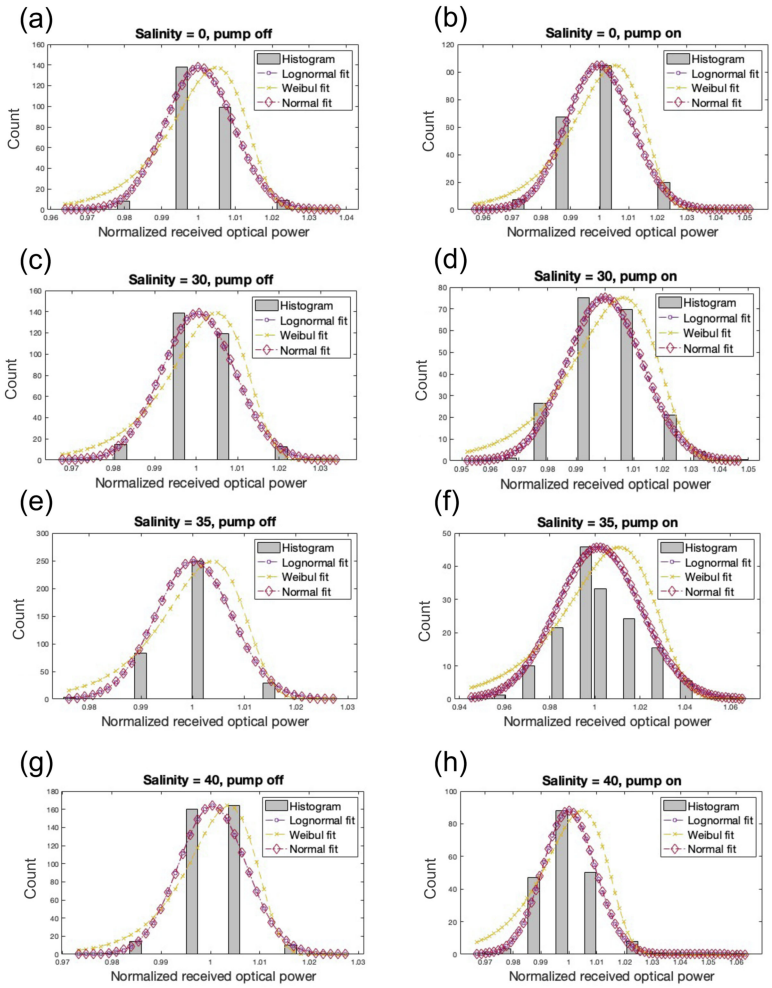

Fig. 8. Acquired data histograms along with different distributions' PDF for various channel scenarios, namely, (a) absence of salinity in still water and (b) turbulent water, (c) uniform salinity of 30‰ in still and (d) turbulent water, (e) uniform salinity of 35‰ in still and (f) turbulent water, and (g) uniform salinity of 40‰ in still and (h) turbulent water.

TABLE II
GOF AND PARAMETERS OF DIFFERENT PDFS FOR UNIFORM SALINITY

Channel	Lognormal (R^2, μ, σ^2)	Weibull (R^2, a, b)	Normal (R^2, μ, σ^2)
0/pump: OFF	0.9943, $1.88e^{-4}$, 0.0074	0.9842, 1.0038, 134.383	0.9950, 1.0002, 0.0074
0/pump: ON	0.8964, 0.0017, 0.0186	0.7320, 1.011, 53.69	0.9950, 1.0018, 0.0168
30/pump: OFF	0.923, $2.86e^{-4}$, 0.0094	0.8034, 1.005, 106.037	0.9950, 1.0003, 0.0093
30/pump: ON	0.9576, -0.0014, 0.0113	0.8673, 1.0043, 88.56	0.9577, 1.0087, 0.0113
35/pump: OFF	0.8627, $7.4e^{-4}$, 0.0177	0.622, 1.001, 54.977	0.8557, 1.0009, 0.0177
35/pump: ON	0.4270, -0.0049, 0.0272	0.1386, 1.009, 37.53	0.4034, 0.9955, 0.0272
40/pump: OFF	0.9728, $-4.56e^{-4}$, 0.0073	0.8693, 1.0032, 137.5	0.9719, 0.9996, 0.0073
40/pump: ON	0.9812, $-1.55e^{-4}$, 0.0086	0.9283, 1.0041, 117.303	0.9804, 0.9999, 0.0086

data bins are lowered. Secondly, with the combination of the first reason and the constant signal level, less data bins are recorded. However, they still preserve enough to samples to be fitted with various distribution curves. We can observe that all histograms seem to fit the normal and lognormal distributions quite accurately, as can be seen from the R^2 values in Table II (the units of the values have been omitted for brevity). However, the Weibull distribution seems to lack accuracy in fitting the experimental data. Secondly, it can be observed that water circulation does not cause deviations in the acquired histograms but increases the variance of the distribution.

Considering the acquired data histograms and the fitted PDFs from the salinity gradient channels in Figs. 9(a)–(h) shows that the normal and lognormal distributions can still adequately describe the channel behavior. Additionally, we can clearly observe from Table III that the variance increases as the water becomes turbulent. Nevertheless, these results indicate that NLOS seawater channels can be statistically predicted, with high confidence, using the normal distribution for all turbulence strengths.

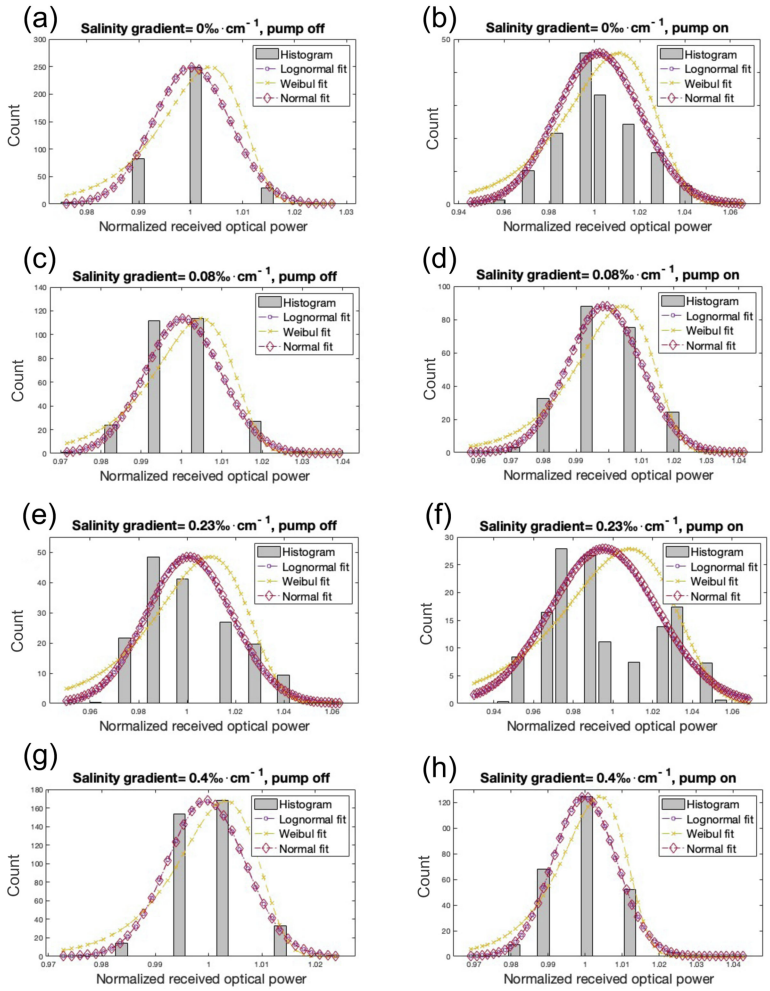

Fig. 9. Acquired data histograms along with different distributions' PDF for various channel scenarios, namely, (a) absence of salinity gradient in still water and (b) turbulent water, (c) salinity gradient of 0.088‰· cm^{-1} in still and (d) turbulent water, (e) salinity gradient of 0.23‰· cm^{-1} in still and (f) turbulent water, and (g) salinity gradient of 0.4‰·cm^{-1} in still and (h) turbulent water.

TABLE III
GOF AND PARAMETERS OF DIFFERENT PDFS FOR GRADIENT SALINITY

Channel	Lognormal (R^2, μ, σ^2)	Weibull (R^2, a, b)	Normal (R^2, μ, σ^2)
0/pump: OFF	0.9821, $1.35e^{-4}$, 0.0093,	0.8086, 1.0049, 103.97	0.9801, 1.0002, 0.0093
0/pump: ON	0.9877, $-2.3e^{-4}$, 0.0113,	0.9466, 1.0054, 86.906	0.9857, 0.9998, 0.0113
0.08/pump: OFF	0.9798, $4.826e^{-4}$, 0.0088	0.8609, 1.0049, 113.79	0.9797, 1.0005, 0.0088
0.08/pump: ON	0.9560, $-1.915e^{-4}$, 0.0132	0.8575, 1.066, 70.7345	0.9574, 0.999, 0.0132
0.23/pump: OFF	0.9944, $1.88e^{-4}$, 0.0074	0.9843, 1.0038, 134.38	0.995, 1.0002, 0.0074
0.23/pump: ON	0.8965, 0.0017, 0.0185	0.7320, 1.011, 3.69	0.8932, 1.0018, 0.0186
0.4/pump: OFF	0.9418, $3.41e^{-4}$, 0.0068	0.8706, 1.0037, 149.94	0.9436, 1.0004, 0.0068
0.4/pump: ON	0.9645, $-2.67e^{-4}$, 0.0094	0.8179, 1.0047, 90.91	0.9617, 1, 0.0094

However, this is not the case in the LOS configuration. The problem with LOS channels is that the strength of fluctuation varies dramatically depending on the turbulence strength. Therefore, each turbulence strength (i.e., from weak to strong) requires its own modeling distribution. For this reason, considerable efforts have been made to unifying the fading statistics and proposing different statistical distributions to describe the channels. For example, salinity-induced turbulence in the LOS configuration was modeled using lognormal, gamma, Weibull, exponentiated Weibull, gamma-gamma, and generalized-gamma distributions depending on the turbulence strength [27], [7], [26]. Therefore, the robustness of the NLOS configuration has been validated to withstand, and even take advantage of, channel impairments. Further research is required to practically enhance this link configuration by considering robust modulation schemes, using highly sensitive solid-state and large-detection-area single-photon receivers in the UV range to achieve long-distance communication.

IV. Conclusion

In this paper, we experimentally demonstrated the robustness of NLOS configurations as a feasible communication link that benefits from underwater channel turbulence to improve the transmission quality. We showed that salt particles in the seawater invoke scattering, so increasing the salt concentration enhances the communication link. We verified our conjecture by studying the PL at different salt concentrations and salinity gradients in homogenous and turbulent channels. Our results showed a PL gain of 2.35 dB/m when the gradient salinity is developed and circulated using a laboratory-emulated turbulent channel. Additionally, we evaluated the communication performance based on the presence of salinity-induced turbulence. Our results were aligned with our predictions, in which increasing the salt concentration and salinity gradient lower the BER. We showed that the increase in the SNR compensates for turbulence causes fading, resulting in overall better performance. Finally, we modeled the NLOS channel using statistical distributions along with all turbulence ranges and found that the normal distribution can adequately describe the fading statistics. Further, we showed that the SNR is strongly correlated with the scintillation index. These results motivate further research on NLOS regimes and the scaling-up of laboratory experiments in existing water bodies such as the ocean.

Acknowledgment

The author Mohammed Sait gratefully acknowledges the beneficial equipment discussion with Dr. Xiaobin Sun.

References

[1] H. Marine, "Submarine cable map," Accessed: Oct. 28, 2021. [Online]. Available: https://www.submarinecablemap.com

[2] H. M. Oubei *et al.*, "Light based underwater wireless communications," *Japanese J. Appl. Phys.*, vol. 57, no. 8S2, 2018, Art. no. 08PA06.

[3] X. Che, I. Wells, G. Dickers, P. Kear, and X. Gong, "Re-evaluation of RF electromagnetic communication in underwater sensor networks," *IEEE Commun. Mag.*, vol. 48, no. 12, pp. 143–151, Dec. 2010.

[4] J. Xu, "Underwater wireless optical communication: Why, what, and how?," *Chin. Opt. Lett.*, vol. 17, no. 10, 2019, Art. no. 100007.

[5] M. V. Jamali *et al.*, "Statistical distribution of intensity fluctuations for underwater wireless optical channels in the presence of air bubbles," in *Proc. Iran Workshop Commun. Inf. Theory*, 2016, pp. 1–6.

[6] Y. Guo *et al.*, "On the reciprocity of underwater turbulent channels," *IEEE Photon. J.*, vol. 11, no. 2, Apr. 2019, Art. no. 7901909.

[7] H. M. Oubei, X. Sun, T. K. Ng, O. Alkhazragi, M.-S. Alouini, and S. B. Ooi, "Scintillations of RGB laser beams in weak temperature and salinity-induced oceanic turbulence," in *Proc. 4th Underwater Commun. Netw. Conf.*, 2018, pp. 1–4.

[8] H. M. Oubei, R. T. ElAfandy, K.-H. Park, T. K. Ng, M.-S. Alouini, and B. S. Ooi, "Performance evaluation of underwater wireless optical communications links in the presence of different air bubble populations," *IEEE Photon. J.*, vol. 9, no. 2, Apr. 2017, Art. no. 7903009.

[9] D. Chen, J. Wang, S. Li, and Z. Xu, "Effects of air bubbles on underwater optical wireless communication," *Chin. Opt. Lett.*, vol. 17, no. 10, 2019, Art. no. 100008.

[10] M. Singh, M. L. Singh, G. Singh, and H. S. Gill, "Statistical channel model for underwater wireless optical communication system under a wide range of air bubble populations," *Opt. Eng.*, vol. 60, no. 3, 2021, Art. no. 036111.

[11] D.-C. Li, C.-C. Chen, S.-K. Liaw, S. Afifah, J.-Y. Sung, and C.-H. Yeh, "Performance evaluation of underwater wireless optical communication system by varying the environmental parameters," *Photonics*, vol. 8, no. 3, pp. 1–12, 2021.

[12] J. Li, J. Luo, S. Li, and X. Yuan, "Centroid drift of laser beam propagation through a water surface with wave turbulence," *Appl. Opt.*, vol. 59, no. 20, pp. 6210–6217, 2020.

[13] G. He, Z. Lv, C. Qiu, and Z. Liu, "Performance evaluation of 520 nm laser diode underwater wireless optical communication systems in the presence of oceanic turbulence," in *Proc. SID Symp. Dig. Tech. Papers*, vol. 51, 2020, pp. 47–50.

[14] M. Yousefi, F. D. Kashani, A. Aghajani, and M. R. H. Rad, "Experimental study of the effects of thermally induced optical turbulence on underwater wireless optical communication link parameters," *J. Opt.*, vol. 22, no. 2, 2020, Art. no. 025702.

[15] S. Kumar, S. Prince, J. Venkata Aravind, and S. Kumar G., "Analysis on the effect of salinity in underwater wireless optical communication," *Mar. Georesources Geotechnol.*, vol. 38, no. 3, pp. 291–301, 2020.

[16] S. Kumar, S. Prince, and G. S. Kumar, "Investigation on effects of system parameters on transmission depth in underwater wireless optical communication," *Photonic Netw. Commun.*, vol. 41, no. 2, pp. 163–176, 2021.

[17] V. Guerra, J. Rufo, J. Rabadan, and R. Perez-Jimenez, "Effect of moving microalgae on underwater wireless optical links," *Appl. Opt.*, vol. 59, no. 2, pp. 515–520, 2020.

[18] Y. Weng, Y. Guo, O. Alkhazragi, T. K. Ng, J.-H. Guo, and B. S. Ooi, "Impact of turbulent-flow-induced scintillation on deep-ocean wireless optical communication," *J. Lightw. Technol.*, vol. 37, no. 19, pp. 5083–5090, 2019.

[19] O. Alkhazragi *et al.*, "Spectrally resolved characterization of thermally induced underwater turbulence using a broadband white-light interrogator," *IEEE Photon. J.*, vol. 11, no. 5, Oct. 2019, Art. no. 7905609.

[20] M. Sait *et al.*, "The effect of turbulence on NLOS underwater wireless optical communication channels," *Chin. Opt. Lett.*, vol. 17, no. 10, 2019, Art. no. 100013.

[21] P. Tian *et al.*, "Absorption and scattering effects of Maalox, chlorophyll, and sea salt on a micro-led-based underwater wireless optical communication," *Chin. Opt. Lett.*, vol. 17, no. 10, 2019, Art. no. 100010.

[22] B. Wozniak and J. Dera, *Light Absorption in Sea Water*. Berlin, Germany: Springer, 2007.

[23] X. Zhang and L. Hu, "Scattering by pure seawater at high salinity," *Opt. Exp.*, vol. 17, no. 15, pp. 12685–12691, 2009.

[24] X. Zhang, L. Hu, and M.-X. He, "Scattering by pure seawater: Effect of salinity," *Opt. Exp.*, vol. 17, no. 7, pp. 5698–5710, 2009.

[25] M. Bernotas and C. Nelson, "Probability density function analysis for optimization of underwater optical communications systems," in *Proc. OCEANS 2015-MTS/IEEE Washington*, 2015, pp. 1–8.

[26] H. M. Oubei *et al.*, "Efficient Weibull channel model for salinity induced turbulent underwater wireless optical communications," in *Proc. Opto-Electron. Commun. Conf. Photon. Glob. Conf.*, 2017, pp. 1–2.

[27] M. V. Jamali *et al.*, "Statistical studies of fading in underwater wireless optical channels in the presence of air bubble, temperature, and salinity random variations," *IEEE Trans. Commun.*, vol. 66, no. 10, pp. 4706–4723, Oct. 2018.

[28] C. Mobley, *Light and Water: Radiative Transfer in Natural Waters*. New York, NY, USA: Academic Press, 1994.

[29] M. Kong *et al.*, "AquaE-lite hybrid-solar-cell receiver-modality for energy-autonomous terrestrial and underwater Internet-of-Things," *IEEE Photon. J.*, vol. 12, no. 4, Aug. 2020, Art. no. 7904713.

[30] X. Sun *et al.*, "375-nm ultraviolet-laser based non-line-of-sight underwater optical communication," *Opt. Exp.*, vol. 26, no. 10, pp. 12870–12877, 2018.

[31] Z. Xu and B. M. Sadler, "Ultraviolet communications: Potential and state-of-the-art," *IEEE Commun. Mag.*, vol. 46, no. 5, pp. 67–73, May 2008.

[32] A. Vavoulas, H. G. Sandalidis, N. D. Chatzidiamantis, Z. Xu, and G. K. Karagiannidis, "A survey on ultraviolet C-band (UV-C) communications," *IEEE Commun. Surv. Tut.*, vol. 21, no. 3, pp. 2111–2133, Jul.–Sep. 2019.

[33] M. Sait, V. Mazzone, and A. Fratalocchi, "Broadband holography via structured black silicon nano-antennas," *Appl. Sci.*, vol. 9, no. 7, 2019, Art. no. 1378.

[34] D. A. Anati, "The salinity of hypersaline brines: Concepts and misconceptions," *Int. J. Salt Lake Res.*, vol. 8, no. 1, pp. 55–70, 1999.